JGR Oceans

RESEARCH ARTICLE
10.1029/2020JC016537

Effects of Source Faulting and Fringing Reefs on the 2009 South Pacific Tsunami Inundation in Southeast Upolu, Samoa

Cyprien Bosserelle[1], Shaun Williams[1], Kwok Fai Cheung[2], Thorne Lay[3], Yoshiki Yamazaki[2], Titimanu Simi[4,5], Volker Roeber[6], Emily Lane[1], Ryan Paulik[1], and Lameko Simanu[4]

[1]Natural Hazards Centre, National Institute of Water and Atmospheric Research (NIWA), Christichurch, Aotearoa New Zealand, [2]Department of Ocean and Resources Engineering, University of Hawaii at Manoa, Honolulu, HI, USA, [3]University of California, Santa Cruz, Santa Cruz, CA, USA, [4]Disaster Management Office, Ministry of Natural Resources and Environment, Apia, Samoa, [5]Now at Management Unit, Green Climate Fund, Samoa Ministry of Finance, Apia, Samoa, [6]E2S Chair HPC-Waves Laboratoire SIAME, Université de Pau et des Pays de l'Adour (E2S UPPA), Anglet, France

Key Points:

- The tsunami water level produced by the 2009 earthquake doublet is simulated for Samoa and compared to observed runup on southeast Upolu
- Geometry of the intraplate normal faulting near the northern Tonga Trench terminus influences the extreme runup on southeast Upolu
- The runup on southeast Upolu is also dependent on fine-scale topographic features and wave excitation over the reef flats

Supporting Information:

- Supporting Information S1

Correspondence to:

C. Bosserelle,
Cyprien.Bosserelle@niwa.co.nz

Citation:

Bosserelle, C., Williams, S., Cheung, K. F., Lay, T., Yamazaki, Y., Simi, T., et al. (2020). Effects of source faulting and fringing reefs on the 2009 South Pacific Tsunami inundation in southeast Upolu, Samoa. *Journal of Geophysical Research: Oceans*, *125*, e2020JC016537. https://doi.org/10.1029/2020JC016537

Received 23 JUN 2020
Accepted 18 NOV 2020

Abstract The subduction zone along the northern Tonga Trench has the highest plate convergence rate in the world, but limited records of its seismic and tsunamigenic activities. In 2009, a tsunami generated by an M_W 8.1 earthquake doublet caused severe impacts in the region including damage and loss of life on the south shores of Upolu and Savaii Islands, Samoa. Here, we use numerical modeling aided by recorded data and eyewitness accounts to evaluate and identify the published source models in the Tonga Trench region that most suitably represent the 2009 event for use in hazard assessment around Samoa. We show that only a few of the published sources are suitable to reproduce the large inundation observed in Samoa, and none reproduces runup as high as observed in the areas that were most severely impacted on the southeast Upolu coast. The distribution and intensity of runup and inundation are dependent on source model, local topographic and bathymetric features, regional coastal geomorphology, and trapping of short-period waves over the reef flats. The computed results are also influenced by model approximation and grid resolution especially for areas with extreme runup records. Comparison of the relative contributions from the doublet to the southeast Upolu inundation indicates that the initial intraplate normal faulting dominated the east-northeastward tsunami propagation and inundation compared with the subsequent interplate thrust faulting. Overall, two key source models are discussed and identified for future refinement.

Plain Language Summary This study models the September 29, 2009 tsunami in Samoa and compares model outputs with tsunami water level observations, field data of runup and inundation as well as eye-witness accounts collected after the event occurred. Whilst several studies have reconstructed the runup and inundation of this event in American Samoa, this is the first time such work has been undertaken in Samoa which lies to the west (formerly known as Western Samoa). We discuss the effects of the complex earthquake sequence that triggered the tsunami event, as well as influence of nearshore coastal characteristics on the pattern and behavior of tsunami impacts observed onshore.

1. Introduction

Tsunami inundation in reef-fringed environments is highly influenced by the characteristics of the source event (e.g., L. Li et al., 2016) as well as the nearshore geomorphology (e.g., Dilmen et al., 2018; Gelfenbaum et al., 2011; Roeber et al., 2010; Tang et al., 2009). Local observations of nearshore and runup processes provide the evidence base for refining and improving source parameters through forward tsunami modeling (e.g., Davies, 2019; Yamazaki et al., 2018). Such improvements can lead to more realistic tsunami hazard representations and a better understanding of local processes for use in coastal management planning.

The September 29, 2009 South Pacific Tsunami (2009 SPT) initiated from an M_W 8.1 earthquake sequence involving nearly simultaneous (within 2 min of each other) intraplate normal faulting in the outer rise oceanic plate and major interplate reverse faulting (M_W 8.0) (Beavan et al., 2010; Fan et al., 2016; Hossen

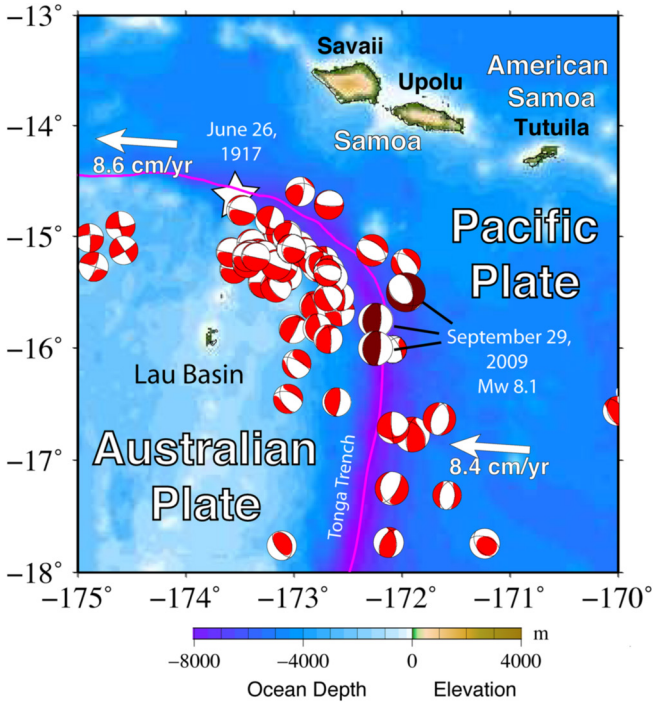

Figure 1. The northern Tonga subduction zone and the major Samoan Islands. The Pacific Plate underthrusts the Tonga block of the Australian Plate along the Tonga Trench. Spreading of the Lau Basin back-arc increases the convergence rate across the Tonga Trench to about 25 cm/yr in this region. The moment tensor solutions from the Global Centroid Moment Tensor catalog for $M_W \geq 6.0$ from 1976 to 2020 are shown. The star indicates the estimated location of the June 26, 1917 ($M_W \sim 8.0$) earthquake (ISC-GEM). The September 29, 2009 event involved an M_W 8.1 outer-rise normal faulting and two interplate thrust faulting events with a combined M_W 8.0 (Lay et al., 2010).

et al., 2017; Kiser & Ishii, 2012; Lay et al., 2010). The USGS-NEIC epicenter (15.489°S, 172.095°W) for this M_W 8.1 event is located 150 km southeast of the 1917 $M_W \sim 8.0$ event (Figure 1). The combined faulting generated a tsunami across the South Pacific that caused widespread inundation, damage and loss of life on the southern coasts of Upolu and Savaii Islands in the Independent State of Samoa (herein Samoa), Tutuila Island in American Samoa, and Niuatoputapu Island in northern Tonga (Clark et al., 2011; Goff & Dominey-Howes, 2011; E. A. Okal et al., 2010; Wilson et al., 2009).

In the aftermath of the event, extensive investigation of the tsunami source and wave characteristics were undertaken based on seismic and GPS records, field surveys, and numerical modeling (e.g., Beavan et al., 2010; Dilmen et al., 2018; Fan et al., 2016; Goff & Dominey-Howes, 2011; Han et al., 2019; Hossen et al., 2017; Lay et al., 2010; E. A. Okal et al., 2010; Roeber et al., 2010; Williams, 2019; Wood et al., 2018; Yamazaki et al., 2011; Zhou et al., 2012). Previous efforts to reconstruct tsunami characteristics in Samoa were limited to simulating wave initiation and propagation up to the reef edge (e.g., Franchello & Annunziato, 2012; Fritz et al., 2011; E. Okal et al., 2011; Zhou et al., 2012). Shoreward wave propagation and inundation was not previously addressed due to lack of high-resolution topography and nearshore bathymetry for this region. Recent acquisition of high-resolution Light Detection and Ranging (LiDAR) topography and nearshore bathymetry (FUGRO, 2016) now enables re-evaluation of the event; modeling the tsunami initiation, propagation, and inundation along southeast Upolu, Samoa.

This paper reconstructs the 2009 SPT through numerical modeling to study the characteristics of wave initiation, propagation, and inundation in Samoa, with emphasis on the observed runup particularly on southeast Upolu Island. This coastline experienced the highest observed runup, flow depths, damage and loss of life in Samoa (E. A. Okal et al., 2010). We assess whether current understanding of the rupture mechanism and propagation explains the extreme runup and flow depths observed in this region. We test rupture source mechanisms compiled by Fan et al. (2016), Hossen et al. (2017), and Han et al. (2019) against the Deep Ocean Assessment and Reporting of Tsunami (DART) data closest to the source, Apia tide gauge measurements, and runup measurements from post-disaster surveys (e.g., Dudley et al., 2011; E. A. Okal et al., 2010, E. Okal et al., 2011; Reese et al., 2011).

We consider 14 source representations of the 2009 SPT that are adapted from published models. The overall objective is to compare and evaluate the 14 source representations with respect to the observed waveforms, inundation, and runup for future refinement (e.g., finite-fault models) and use in hazard exposure and impacts assessment. The importance of validating models with surveyed runup, as well as quantifying the effects of coastal topography on wave behavior, are discussed.

2. Regional Context and Setting

The Samoan archipelago, comprising of Samoa and American Samoa, is situated along a volcanic hotspot island chain (Koppers et al., 2008), ~100 km north of the terminus of the Tonga Trench. The tectonics and seismicity of this region are illustrated in Figure 1. The Pacific Plate undergoes strong deformation as it subducts steeply beneath the Tonga Arc, while north of the hook-like terminus the plate continues westward. The bending and tearing of the plate at the terminus (e.g., Govers & Wortel, 2005; Millen & Hamburger, 1998) coupled with mantle plume upwelling (e.g., Chang et al., 2016; Konter & Jackson, 2012; Koppers et al., 2011), produces complex strain and faulting that results in significant seismic hazard for the Samoan archipelago (e.g., Gurnis et al., 2000; Fan et al., 2016). The average convergence rate of 25 cm/yr between the

Pacific Plate and the overriding Tonga block is the highest among all subduction zones (Bassett et al., 2016; Bevis et al., 1995). The rate is enhanced by rapid back-arc spreading of the Lau Basin combined with roll-back of the subduction zone (Chang et al., 2016).

Despite the high convergence and seismicity rate (Bassett et al., 2016), recorded interplate thrust faulting activity only involves events with magnitudes up to ~8.0 (e.g., Meng et al., 2015). Intraplate earthquakes within the deformed Pacific Plate, such as the June 26, 1917 Samoa (M_m 8; M_S 8.7) and 2009 Samoa-Tonga earthquakes located along the bend in the arc (Figure 1), are the largest recorded seismic events in the region (e.g., Meng et al., 2015; E. Okal, 1992) and both have triggered major tsunamis (E. Okal et al., 2011).

There is general agreement that the overall source of the 2009 SPT involved both interplate thrust-faulting and intraplate normal-faulting. Beavan et al. (2010) used campaign geodetic observations and approximate tsunami arrival time reports to infer that a slow tsunami-earthquake on the plate boundary interface triggered trench-slope intraplate normal-faulting. Lay et al. (2010) used regional and teleseismic waveform modeling to develop a model where intraplate normal-faulting occurred first, triggering interplate thrusting events 49 and 90 s after the initial rupture, with the timing of all large moment release well constrained by the seismic signals. Analysis of two-event centroid moment tensor solutions by Duputel et al. (2012), Nealy and Hayes (2015), and Fan et al. (2016) support the latter interpretation, but the possibility of a precursory weak, very long-duration initial slip event on the thrust plane has not been ruled out. Modeling of seismic waves for the intraplate normal faulting has invoked either a southwestward dipping plane (e.g., Lay et al., 2010; Nealy & Hayes, 2015) or an east-northeastward dipping plane (e.g., Beavan et al., 2010; Fan et al. 2016; X. Li et al., 2009; Nealy & Hayes, 2015). The latter orientation is compatible with modeling of the reconstructed tsunami source area (e.g., Hossen et al., 2017) and with models of geodetic and gravity changes including viscoelastic relaxation (e.g., Han et al., 2019). However, the precise strike and dip of either candidate fault plane is ambiguous because of frequency dependence of the long-period point-source moment tensors and their associated best-double couple fault plane candidates (Lay et al., 2010). Modeling an eastward dipping normal fault implies an increased slab dip and dominance of the oceanic plate bending moment relative to decreased in-plane force, and greater extensional in-shear stress causing a negative dynamic topography response seaward of the trench axis (e.g., Craig et al., 2014).

While detailed orientation and timing of the complex faulting is not fully resolved, there is agreement that the resulting tsunami was triggered by both normal and reverse faulting. Roeber et al. (2010) attributed the impacts of the tsunami along the shores of Tutuila Island (American Samoa), which lies ~97 km east of Upolu, to shelf resonance and tsunami amplification at the natural periods of bathymetric features. The near-shore bathymetry, generally characterized by steep slopes and narrow reef morphology on the insular shelf, was suggested to modulate the incident tsunami waves resulting in varying flow conditions around the island. Wood et al. (2018) later showed that multiple waves with similar amplitudes impacted most locations in American Samoa rather than a single large wave. Nevertheless, fringing reef morphology and narrow embayments are important factors in explaining the variations in runup and flow depth on Tutuila (Dilmen et al., 2015, 2018; Gelfenbaum et al., 2011; Roeber et al., 2010). In Samoa, such analysis of wave characteristics relative to observed runup and inundation has not previously been carried out and is the focus of this paper.

3. Methods and Data

3.1. Model Configuration and Grid Scheme

The shock-capturing hydrodynamics model BG-Flood (Block-adaptive on Graphics processing unit Flood model) is used to reconstruct the 2009 SPT from the seismic source to inundation (Figure 2). BG-Flood simulates shallow water hydrodynamics on graphics processing units (GPU) using a nested grid system. The model governing equations are from the Saint-Venant, shallow water equation (SWE) solver in Basilisk (Popinet, 2011), but uses a Block Uniform Quadtree mesh that runs efficiently on GPU (e.g., Vacondio et al., 2017). The SWE engine is well established and tested in Basilisk through tsunami benchmark evaluation, with the solver and its ability to define propagation and inundation as described by Popinet (2012). The model, however, does not include dispersive terms (present in Boussinesq-type or nonhydrostatic models). While the hydrostatic model is well suited for testing the range of source scenarios to identify which are the

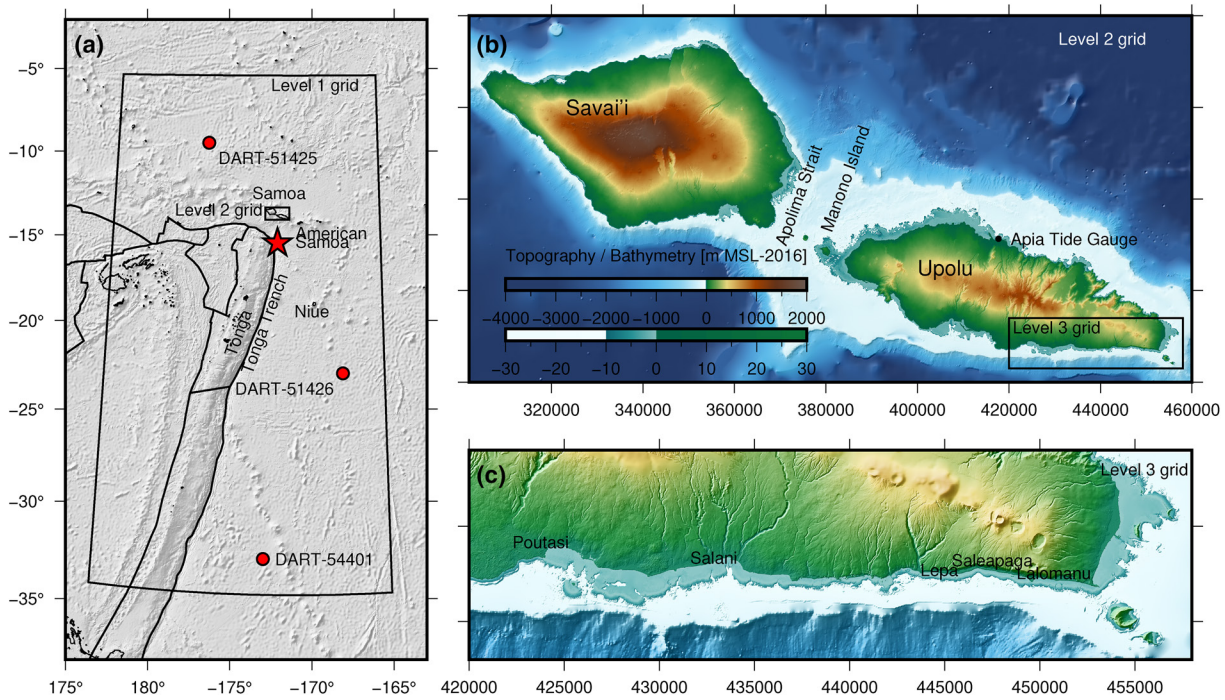

Figure 2. The model region for the 2009 South Pacific Tsunami. (a) Regional view with level-1 (250 m resolution) and level-2 (50 m resolution) computational domain outlined in black and DART buoy locations (red circles). Red star indicates epicenter. (b) Level-2 computational domain showing the insular shelves of the Samoan Islands, the Apia tide gauge, and outline of the level-3 computational domain. (c) Level-3 computational domain showing the nearshore fringing reef system within the insular shelves on southeast Upolu. DART, Deep Ocean Assessment and Reporting of Tsunami.

most representative of the observed inundation and runup, it may not be capable of reproducing some of the short-period tsunami waves and their nearshore behavior in insular shelf and reef environments (Bai & Cheung, 2016).

The BG-Flood model is configured using three nested uniform Cartesian grids to simulate the 2009 SPT propagation from initiation to inundation (Figure 2). The level-1 grid extends across the northern region of the Tonga subduction zone at a resolution of 250 m to capture wave propagation at DART 51425, DART 51426, and DART 54401 as well as around the Samoan Islands. The level-2 grid resolves tsunami inundation on Upolu, Manono (immediately west of Upolu) and Savaii Islands at 50 m resolution for comparison with surveyed runup in these islands (E. A. Okal et al., 2010) and includes the Apia tide gauge. The level-3 grid solves for inundation at 10 m resolution on southeast Upolu for more detailed comparison with surveyed runup in this area (Dudley et al., 2011; E. A. Okal et al., 2010; Reese et al., 2011). The digital elevation models (DEM) used in these simulations were derived from: (1) the Generic Bathymetric Chart of the Oceans at ~900 m resolution; (2) multibeam bathymetry survey over the shelf slopes at a resolution of ~60 m (Kruger & Kramer, 2008); and (3) LiDAR topography and nearshore bathymetry (down to 30 m depth) at a resolution of 5 m (FUGRO, 2016).

3.2. Source Models, Observations Data, and Comparison

Instrumental records (DART buoys and tide gauge data) and runup measurements were used to evaluate the tsunami simulations. Clear signals of the 2009 SPT were recorded at the three DART stations used in this study as well as the Apia tide gauge. Raw DART data were processed using a Gaussian filter with a 216 s window; tsunami spectral density was calculated from the filtered data resampled to a 10 s interval using the Welch's method with a 512-sample window.

For the Apia tide gauge, the tsunami signal was extracted by removing the tide signal from recorded water level. The tide signal was first predicted using the T-tide software (Pawlowicz et al., 2002), and the full tide gauge record from 1993 to 2019.

Surveyed runup and flow depth were first converted to maximum water level for comparisons. For the Samoa (whole country) analysis, 30 maximum water level points were used in Savaii, 127 points in Upolu, and 7 points in Manono. For the southeast Upolu comparison, 65 maximum water level points were available.

Fourteen source scenarios with different rupture parameters, timing, locations, angles, dips and slip were simulated and compared with the open-ocean DART observations, Apia tide gauge record and surveyed runup (Table 1). This includes a modified source, which applies the rupture dimensions and slip of Lay et al. (2010) but with an east-northeast dipping normal fault (e.g., Fan et al., 2016; Hossen et al., 2017). Fault 1 denotes the normal intraplate rupture in the outer rise and faults 2 and 3 correspond to the later interplate thrusting on the plate boundary (Table 1).

Source parameters include the rupture initiation and dislocation rise times to reconstruct the time history of seafloor deformation through the half-space solutions of Okada (1985; 1992) for modeling of tsunami generation. The intraplate rupture occurred below the 6,000 m deep abyssal seafloor, while the water depth above the thrust faulting extends from 2,000 to 7,000 m over the margin. The 8,300 m deep Tonga Trench lies between the locations of the two subevents and played a significant role in modifying the near-field tsunami through wave refraction associated with rapid variation of the propagation speed. This suggests that the timing of rupture sequence and rise time along with rupture duration are critical in accurately simulating interference of tsunami waves from the subevents and the subsequent inundation.

To evaluate how each source model performs for wave propagation and inundation, we compare the index of agreement between the modeled and observed tsunami wave signals at the DART buoys and the Apia tide gauge. We also compare modeled and observed runup, first for the entire Samoa and then for southeast Upolu only. Each scenario was simulated from initiation to propagation to the DART locations for a total of 4.2 h on the level-1 grid. The Samoa inundation grid (level-2) and southeast Upolu grid (level-3) were also run for 4.2 h. The goodness of the fit between computed and observed maximum inundation (i.e., combined runup and maximum flow elevation) is evaluated using the Willmott index of agreement, IoA (Willmott et al., 2012) (Equation 1):

$$IoA = \begin{cases} 1 - \dfrac{\sum_{i=0}^{n}\left|P_i - O_i\right|}{c\sum_{i=0}^{n}\left|O_i - \bar{O}\right|}, when \sum_{i=0}^{n}\left|P_i - O_i\right| \le c\sum_{i=0}^{n}\left|O_i - \bar{O}\right| \\ \dfrac{c\sum_{i=0}^{n}\left|O_i - \bar{O}\right|}{\sum_{i=0}^{n}\left|P_i - O_i\right|} - 1, when \sum_{i=0}^{n}\left|P_i - O_i\right| > c\sum_{i=0}^{n}\left|O_i - \bar{O}\right| \end{cases} \quad (1)$$

where O_i is the measured data, P_i is the simulated data, the over bar denotes the average, and $c = 2$. As general guidance when comparing the complex and variable nature of tsunamis with idealized simulations, a negative IoA is poor agreement, IoA < 0.25 is weak agreement, IoA > 0.5 is good agreement and IoA > 0.8 is excellent agreement. IoA provides an objective measure of model agreement that is consistent between scenarios and to some degree between datasets.

3.3. Simulation and Computation

The simulation applies the Apia tide level at the time of initiation but does not include the tide variation throughout the simulation. Tide levels around Upolu are assumed to be similar to that at Apia. With the most intense wave action occurring within the first hour after the earthquake the tidal variation is not expected to influence the tsunami significantly. Each grid is nested one-way at a 1 s interval. Outputs at the DART locations and Apia tide gauge are extracted at the model computational time step (~0.7 s at the DART buoys and ~0.1 s at the tide gauge). Maximum water levels and flow depths are updated at each step and compared with observations data from E. A. Okal et al. (2010).

A uniform quadratic bottom roughness ($cf = 0.0001$) was applied to the 250 and 50 m grids. For the level-3 grid, the roughness formulation of Smart (2017) is used. This is related to the Manning formulation but is also valid for very small flow depths with a depth-independent roughness length (z_0). A simple spatially varying roughness map with low roughness length ($z_0 = 0.0001$ m) was applied to elevations lower than 15 m below mean sea level, and a high roughness length ($z_0 = 0.01$ m) used for all other areas including coral

Table 1
Fault Parameters for the Main Scenarios Tested for Runup in Southeast Upolu

No.[a]	Length (km)	Width (km)	Strike angle (°)	Dip angle (°)	Rake angle (°)	Slip (m)	Centroid of rupture			Rupture initiation (s)[b]	Rise time (s)
							Depth (km)	Long. (°W)	Lat. (°S)		
X. Li et al. (2009)											
1	130	50	340.7	45.4	−46.3	4.3	12	172.5	15		15.7
2	50	50	183.7	13.9	69.3	15.8	10	172.5	16.1	91.6	50.8
Beaven et al. (2010)											
1	130	50	352	53	−32	3.1	12	172.2	15.5	0.0	0.0
2	50	50	173	16	75	11.2	12	172.8	16	30	20
Lay et al. (2010) (Version A)											
1	130	50	152.0	67.0	−77.0	6.1	18	172.0	15.5	3.0	60.0
2	50	50	185.0	29.0	90.0	5.6	18	172.4	16.0	49.0	40.0
3	50	50	185.0	29.0	90.0	5.6	18	172.4	16.0	90.0	40.0
Lay et al. (2010) (Version B)											
1	130	50	144.0	65.0	−91.0	6.1	18	172.0	15.5	3.0	60.0
2	50	50	185.0	29.0	83.0	4.7	18	172.3	15.8	49.0	40.0
3	50	50	185.0	29.0	83.0	4.4	18	172.3	16.0	90.0	40.0
Lay et al. (2010) (Version C)[c]											
1	130	50	324.0	65.0	−85.0	10.2	18	172.0	15.5	3.0	60.0
2	50	50	175.0	29.0	90.0	4.7	18	172.4	16.0	49.0	40.0
3	50	50	180.0	29.0	90.0	4.7	18	172.4	16.0	90.0	40.0
Lay et al. (2010) (Version D)[c]											
1	110	35	340	35	265	6.0	15.2	172.00	15.50	3.0	60.0
2	50	75	175	20	90	4.62	17.8	172.70	15.78	49.0	40.0
3	50	75	180	20	90	4.71	17.8	172.68	16.27	90.0	40.0
Lay et al. (2010) (Version E)[c]											
1	110	35	320	35	265	6.0	15.2	172.00	15.50	3.0	60.0
2	50	75	175	20	90	4.62	17.8	172.70	15.78	49.0	40.0
3	50	75	180	20	90	4.71	17.8	172.68	16.27	90.0	40.0
Duputel et al. (2012)											
1	130	50	157.0	64.0	−70.0	4.8	16	172.2	15.1	32.4	53.6
2	50	50	176.9	10.9	79.4	13.3	16	172.7	16.3	105.4	40.0
Nealy and Hayes (2015) (Version F)											
1	130	50	349.9	45.9	−84.6	9.2	16	172.2	15.2	33.0	66.0
2	50	50	158.1	39.6	51.7	19.5	16	172.2	15.2	45.0	80.0
Nealy and Hayes (2015) (Version U)											
1	130	50	356.0	40.1	−78.5	9.6	31	171.8	15.6	33.0	66.0
2	50	50	162.4	47.1	57.9	20.2	24	171.9	15.5	45.0	80.0
Nealy and Hayes (2015) (Version T)											
1	130	50	330.0	44.0	−81.0	4.3	18	172.1	15.5	25.0	50.0
2	50	50	178.5	18.0	59.0	14.3	18	172.9	16.4	91.0	182.0
Nealy and Hayes (2015) (Version C)											
1	130	50	153.0	61.5	−81.6	4.8	18	171.9	15.4	3.0	60.0
2	50	50	171.3	23.5	51.1	12.0	18	172.2	15.5	49.0	40.0

Table 1
Continued

No.[a]	Length (km)	Width (km)	Strike angle (°)	Dip angle (°)	Rake angle (°)	Slip (m)	Centroid of rupture Depth (km)	Long. (°W)	Lat. (°S)	Rupture initiation (s)[b]	Rise time (s)
					Fan et al. (2016)						
1	130	50	344.0	72.0	−68.0	4.3	12	172.2	15.0	0.0	70.0
2	50	50	183.0	15.0	40.0	15.8	12	172.5	16.1	80.0	80.0
					Hossen et al. (2017)						
1	130	50	315.0	25.0	−99.0	6.1	18	172.0	15.5	3.0	60.0
2	50	50	180.0	29.0	90.0	7.9	18	172.4	16.0	49.0	40.0

Note. Fault parameters from original publications (length, width, and slip) have been modified to produce comparable output.

[a]Fault 1 normal fault; Fault 2 reverse fault; Fault 3 reverse fault. [b]Initial rupture in seconds after the earthquake time (2009-09-29, 17:48:10 UTC). [c]Source mechanisms were modified from Lay et al. (2010) using earlier (unpublished) tsunami propagation simulations by some of the co-authors.

reefs, vegetated land, and built environment. This is reasonable given the relatively low density of buildings and infrastructure along the southeast Upolu coastline.

4. Results and Interpretation

4.1. Comparison of Different Sources

The simulation of 14 different sources from tsunami generation to inundation provides a wide range of scenarios whose characteristics are compared with observations. The index of agreement of simulated tsunamis against observations (Table 2) as well as visual comparison of tsunami wave signals at DART buoys and the Apia tide gauge (Figures S1–S14) are used to summarize the results.

None of the 14 sources produce excellent agreement with IoA exceeding 0.8 and no sources produce consistently good agreement against the DART data, the tide gauge and the runup data (Table 2). Sources labeled Lay et al. (2010) Versions D and E, as well as Nealy and Hayes (2015) Version T produce moderate to good agreements at the two closest DART buoys as well as the Apia tide gauge but do not reproduce the observed runup in South East Upolu. On the other hand, Lay et al. (2010) Version C, a modified iteration of Lay et al. (2010) Version B for testing in this study, and Hossen et al. (2017) produce good agreement with observed runup but cannot reproduce the DART and tide gauge as well as other sources. With the DART buoys located far away from the main impact of the tsunami and recording waves in the order of 0.05 m, we deem it more important for a hazard assessment to better match the Apia tide gauge recording (~1.0 m tsunami) and runup (up to 15 m above mean sea level).

Overall Hossen et al. (2017) and Lay et al. (2010) Version C, while imperfect, are most consistent with the observed tsunami data. These two sources are described further in the sections below.

4.2. Propagation

BG-Flood simulates the full complexity of the rupture sequence in the tsunami generation to reconstruct the near-field wave pattern. The computed water levels for Lay et al. (2010) Version C are shown in Figure 3 at key moments after the rupture initiation (see also Movie S15). The normal faulting generates a sea surface trough of 3 m heading to the northeast, while the uplift of the thrust faults adds to the southwest traveling positive wave from the normal fault to produce a surface pulse of 3.8 m amplitude. The relative position of the faults determines the radiated wave pattern across the ocean. The trough generated by the normal faulting reaches Upolu 11 min after the earthquake. It is immediately followed by a positive wave from upswing of the initial surface depression and a larger and broader wave generated by the thrust faulting (Figure 3).

Table 2
Evaluation of the Main Scenarios Against Offshore and Nearshore Tsunami Observations

Study	DART-51425	DART-51426	DART-54401	Apia tide gauge	Samoa runup	Southeast upolu runup
X. Li et al. (2009)	0.27	0.33	0.43	0.47	0.52	0.23
Beaven et al. (2010)	0.36	0.4	0.41	0.55	0.4	0.13
Lay et al. (2010) (Version A)	0.33	0.39	0.46	0.16	0.56	0.35
Lay et al. (2010) (Version B)	0.37	0.44	0.47	0.36	0.61	0.40
Lay et al. (2010) (Version C)	0.21	0.14	0.2	0.22	0.67	0.56
Lay et al. (2010) (Version D)	0.48	0.48	0.47	0.49	0.45	0.14
Lay et al. (2010) (Version E)	0.48	0.47	0.46	0.41	0.6	0.37
Duputel et al. (2012)	0.25	0.36	0.40	0.36	0.51	0.19
Nealy and Hayes (2015) (Version F)	−0.21	0.10	0.36	0.26	0.51	0.61
Nealy and Hayes (2015) (Version U)	0.13	0.13	0.42	0.42	0.64	0.55
Nealy and Hayes (2015) (Version C)	0.21	0.28	0.43	0.54	0.5	0.20
Nealy and Hayes (2015) (Version T)	0.33	0.37	0.35	0.30	0.45	0.17
Fan et al. (2016)	0.18	0.17	0.39	0.40	0.56	0.24
Hossen et al. (2017)	0.38	0.41	0.49	0.25	0.63	0.52

Note. The evaluation is given as the IoA calculated as in Equation 1.
Abbreviation: DART, Deep Ocean Assessment and Reporting of Tsunami.

The second wave crest reaching the shore of southeast Upolu is augmented by reflection of the first to produce the highest water level 19 min after the earthquake, while standing waves gradually develop over the wider shelf to the west producing a large peak 9 min later. The wave pattern is reversed with a leading crest followed by a deep trough toward the west and south. The maximum surface elevation in Figure 3 shows a complex pattern with focusing of the waves behind islands and seamounts in the general propagation direction.

Tsunami simulations using both Lay et al. (2010) Version C and Hossen et al. (2017) adequately reproduce the arrival time at both the DARTs and tide gauge. Computed and recorded waveforms and spectra at the three DART buoys and the Apia tide gauge for these scenarios are shown in Figure 4. The amplitudes of the DART observations are overpredicted which is possibly due to the lack of dispersion in the model. However, the waveform at Apia tide gauge is well modeled, although the amplitude is also overpredicted. Comparisons for other models are shown in Figures S1–S14.

DART 51425 (northwest of the epicenter) and the Apia tide gauge (northeast of the epicenter) both recorded a leading trough from the normal faulting in the outer rise. At DART 51426 (southeast of the epicenter), a leading crest followed by a deep trough from the combined thrust and normal faulting was recorded. The comparison with the DART and Apia tide gauge records corroborates the work of Dilmen et al. (2018) and Wood et al. (2018) in which a leading trough was observed at the Pago Pago Tide Gauge in Tutuila and at DART 51425 in the north, and a leading crest at DART buoys 51426 and 54401 south of the epicenter.

4.3. Runup and Inundation

Simulated runup below 5 m broadly agrees with the observations using both the modified Lay et al. (2010) Version C and Hossen et al. (2017) source models for the level-2 and level-3 grids (Figure 5). For the level-2 grid, observed runup between 5 and 9 m appears to be better captured in the Lay et al. (2010) Version C scenario. The overall agreement between the simulated and observed runups at most locations in Samoa, with the exception of southeast Upolu, indicates general validity of the source models.

In southeast Upolu, comparison between simulated and observed runup (Figures 5 and 6) shows the variable response of the tsunami along the shore. Some scenarios indeed produce high runup where observed.

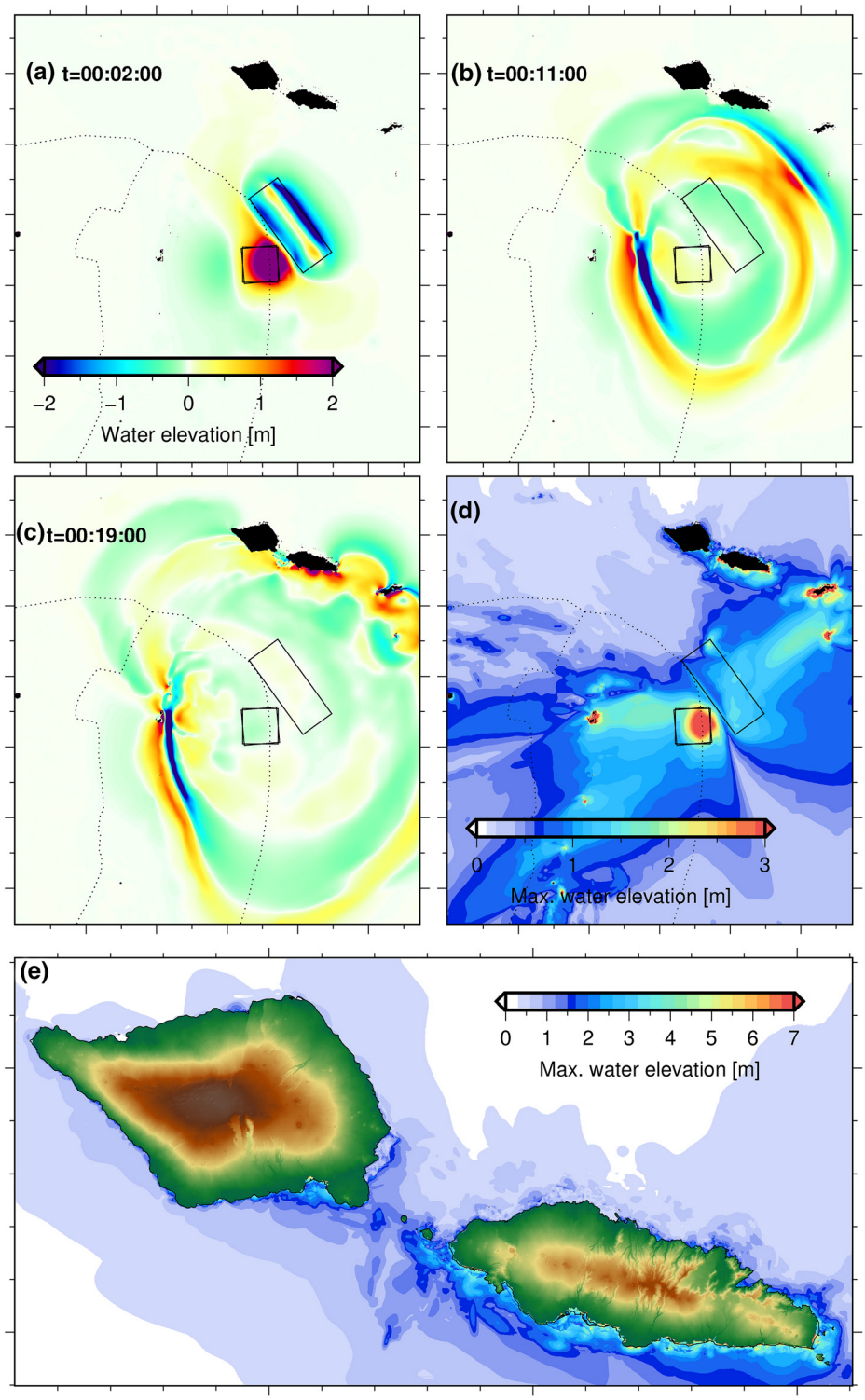

Figure 3. Snapshots of computed sea surface elevation after earthquake initiation, regional maximum surface elevation, and inundation. The relative position of the initial surface disturbances gives rise to a trough leading the tsunami waves toward the north and east and a leading crest to the west and south. (a) Completion of the 3-fault rupture sequence (Faults 2 and 3 have overlapping locations), note the wave generated from the normal fault is already bouncing back to a positive wave and the thrust faulting adding to the initial crest of the normal fault. (b) Arrival of the leading trough at coast on southeast Upolu. (c) Arrival of the combined first crest at coast on southeast Upolu. (d) Regional maximum surface elevation. (e) Maximum inundation in the Samoan islands at 50 m resolution with the mean sea level shoreline represented by the thin black line.

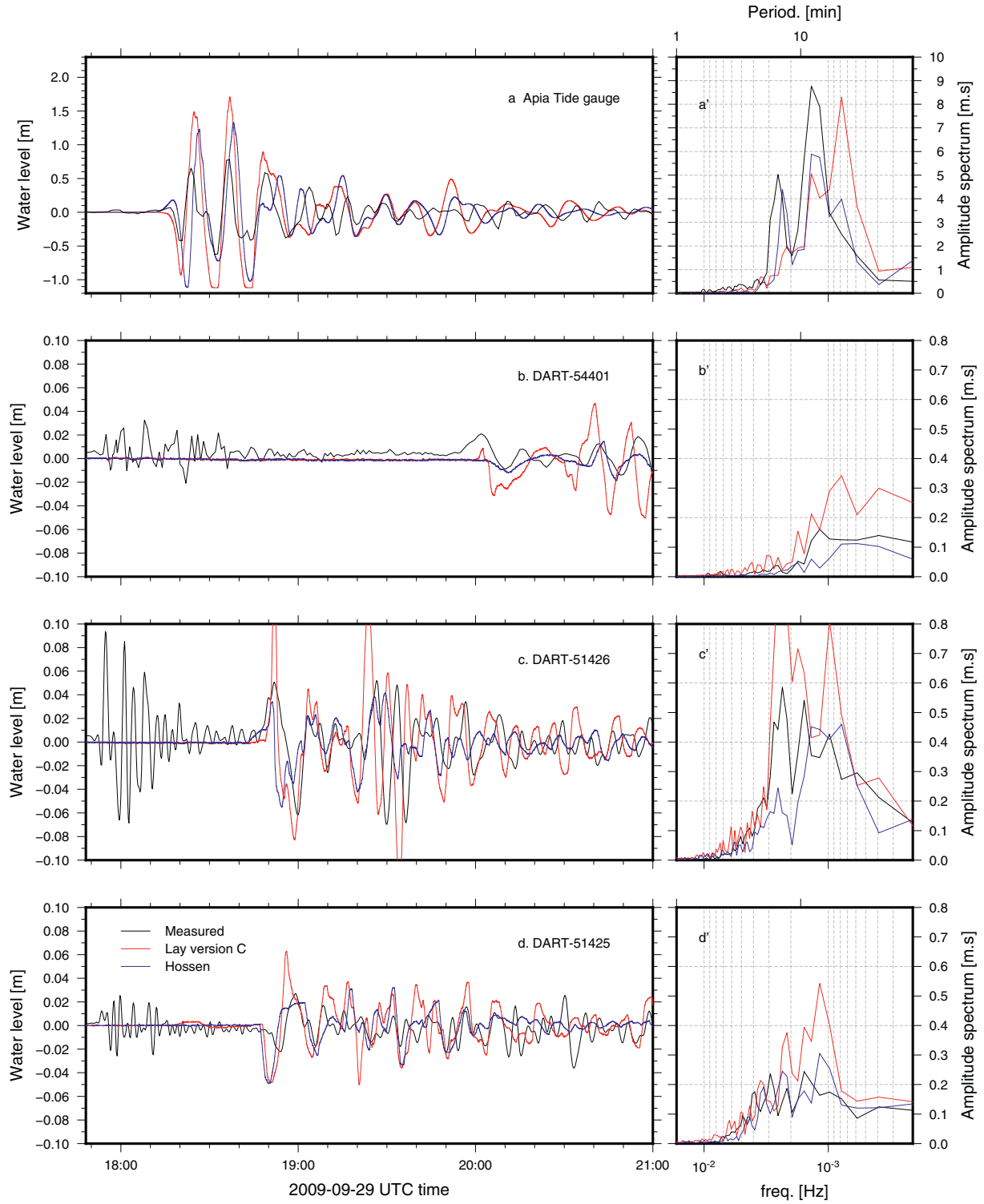

Figure 4. Comparison of recorded (black) and computed (red) time series and spectra of surface elevations at DART water-level stations and the Apia tide gauge. The model reproduces the leading trough at DART 51425 to the north and the leading crest at DART 51426 to the south to confirm the two-stage rupture sequence. Simulated and recorded spectral amplitude are reasonably similar in all four gauges. DART, Deep Ocean Assessment and Reporting of Tsunami.

However, none of the 14 scenarios tested reproduce the extreme runup of 10–15 m on southeast Upolu. These extreme runups occurred east of Lepa, at the apex of Saleapaga bay and on the Lalomanu cliffs. Simulated maximum water levels show "spikes" in the same area of the observed extreme runups suggesting

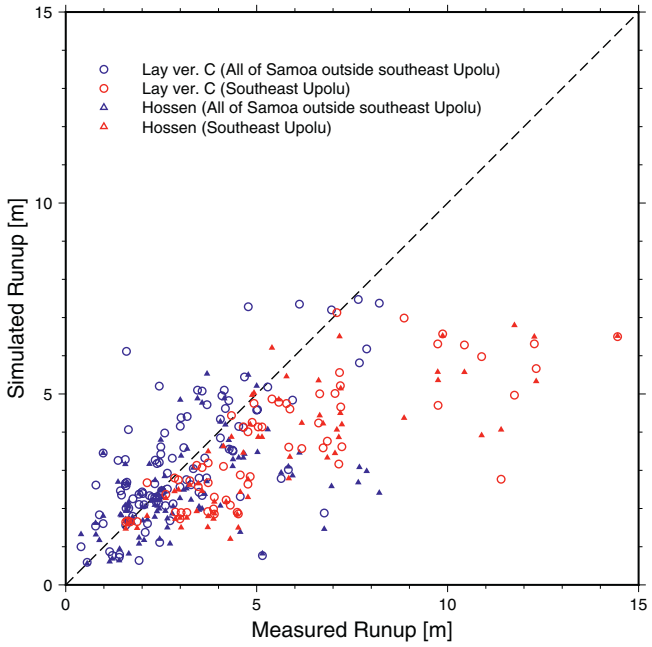

Figure 5. Comparisons of measured and computed runup for the whole of Samoa (blue symbols) and southeast Upolu (red symbols) for the two scenarios by Hossen et al. (2017) (triangles) and Lay et al. (2010) Version C (circles).

that these were caused by highly localized amplification of the incoming tsunami waves over topographic features. In addition, Figure 3 shows the tsunami approaching the area with a large leading trough followed closely by a crest in the form of an *N* wave. A nonhydrostatic model, which includes vertical inertia for flows on steep slopes, might be needed to dynamically describe the initial drawdown and the subsequent upswing to augment the crest arrival in producing the observed extreme runups (Bai et al., 2018).

Trapping and slow drainage of the initial wave within the narrow lagoon appear to provide a higher baseline for subsequent incoming waves to ride in on causing higher flow depths along this coast compared with other locations which were inundated. While southeast Upolu exhibits the highest overall runup in each scenario, the inability of any of the source models to reproduce the extreme runup peaks could be explained by a number of causes: (1) potential limitations of the level-3 resolution in representing 2009 topography and bathymetry in the near- and on-shore; (2) complexity in the source mechanism which is not captured using uniform slip models (e.g., heterogenous slip); (3) dispersion of propagating waves that leads to better alignment with the resonance periods of the locations of extreme runup; and/or (4) vertical flow inertia that might be needed to dynamically model the drawdown and runup process on the steep slope. Nevertheless, the computed maximum runup for Lay et al. (2010) Version C and Hossen et al. (2017) scenarios are generally consistent with recorded observations on all three islands, and consistent with eye-witness accounts in southeast Upolu whereby the second and third waves were generally observed to be the largest (E. Okal et al., 2011; Dudley et al., 2011).

The simulation of the Lay et al. (2010) Version C and Hossen et al. (2017) scenarios confirms the large variation observed in runups and flow depths along the shore at Lepa and Saleapaga. Figure 7 shows the time histories of the flow at these locations. Waves at the shoreline transform from a single peak reaching 6 m elevation at Saleapaga to a single peak of 4 m in Lepa 700 m to the west. A double peak exceeding 5 m is observed 1,000 m further west of Lepa. The waves around Saleapaga appear to have excited the local resonant frequencies over the reef flats (e.g., Abe, 2011), and show the strongest onshore wave energy at these frequencies. The results are consistent with relatively large flow depths up to 6 m observed in this area (Figure 6b) (E. A. Okal et al., 2010). The strongest offshore energy signal observed at lower frequency from the initial pulse and higher onshore energy peaks at lower frequencies are probably due to interference and excitation over the reef flats and insular shelves (e.g., Buckley et al., 2018; Cheung et al., 2013; Gawehn et al., 2016; Gelfenbaum et al., 2011).

5. Discussion

5.1. Complex Source in Complex Bathymetry

The 2009 SPT was unusual because it was triggered by an intraplate-interplate sequence of earthquake rupture. The subsequent tsunami waves were transformed and trapped over complex bathymetric features with significant amplification as they reached and inundated the Samoa shorelines. The high resolution of the simulation presented here reveals significant transformation of the tsunami waves as they reach the complex reef bathymetry.

While the highest modeled runups of ~9 m is below the extreme values of 10–15 m observed on southeast Upolu, the agreement on the rest of this coast is reasonably good. Extreme wave amplification and runup between Lalomanu and Salani on southeast Upolu might be caused by very localized topographic features (e.g., incisions and gullies) at the edge and inside of the narrow fringing reef morphology. These would

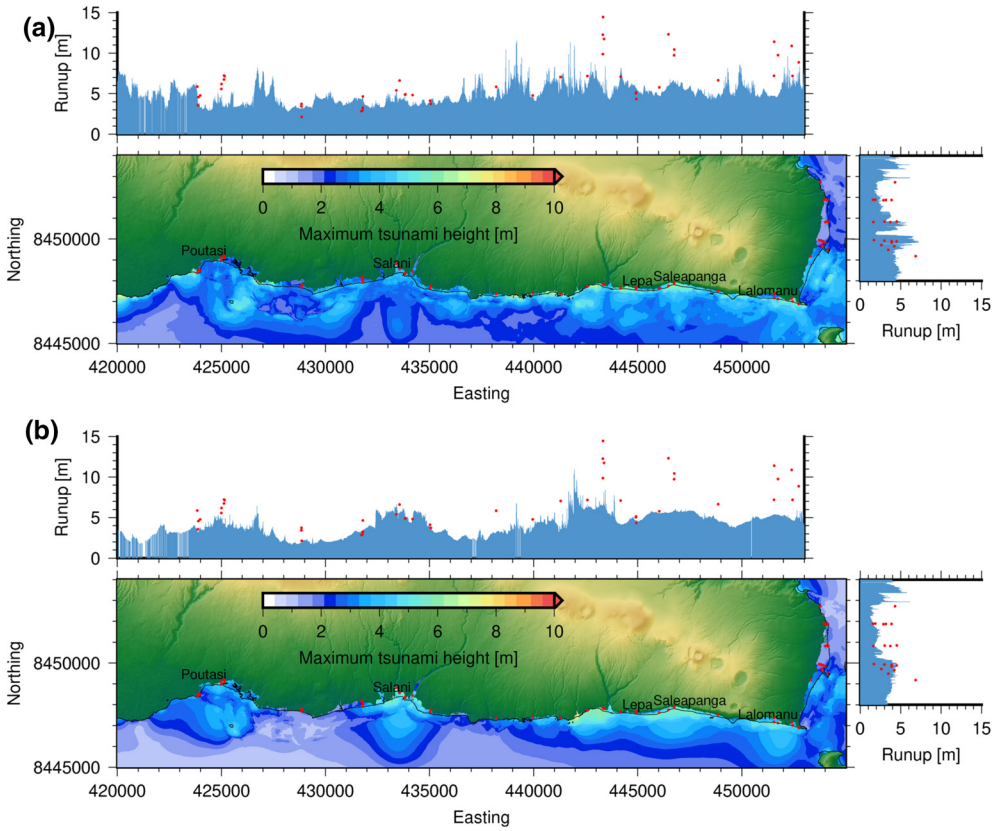

Figure 6. Comparisons of computed with observed inundation on southeast Upolu using (a) Lay et al. (2010) Version C and (b) Hossen et al. (2017).

focus tsunami energy toward adjacent shorelines and exacerbate runup by trapping energy between the reef and the onshore cliff (Figure 8). Interference and convergence between reflected and incoming waves explain the local amplification and runup heights along the southeast coast. Roeber et al. (2010) and Dilmen et al. (2018) modeled similar amplifications due to nearshore reefs in Tutuila exciting resonant modes of 2–4 min on the insular shelf surrounding American Samoa. Our results show that the relatively small change in the incoming tsunami waves and interaction with the narrow reef morphology played a key role in amplifying the 2009 SPT on southeast Upolu.

In general, these observations support suggestions that high-frequency tsunami waves on reef flats (e.g., Gawehn et al., 2016), as well as geomorphologic configuration and fine-scale topographic features within

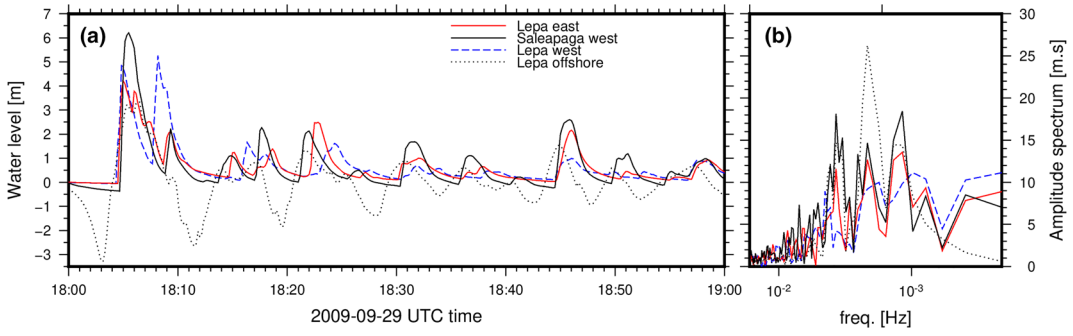

Figure 7. (a) Time series of water level for scenario Lay et al. (2010) Version C showing the variability of onshore hydrodynamics response at Lepa and Saleapaga, and offshore of Lepa. (b) Amplitude spectrum showing local variability of onshore and offshore wave energy and excitation frequencies.

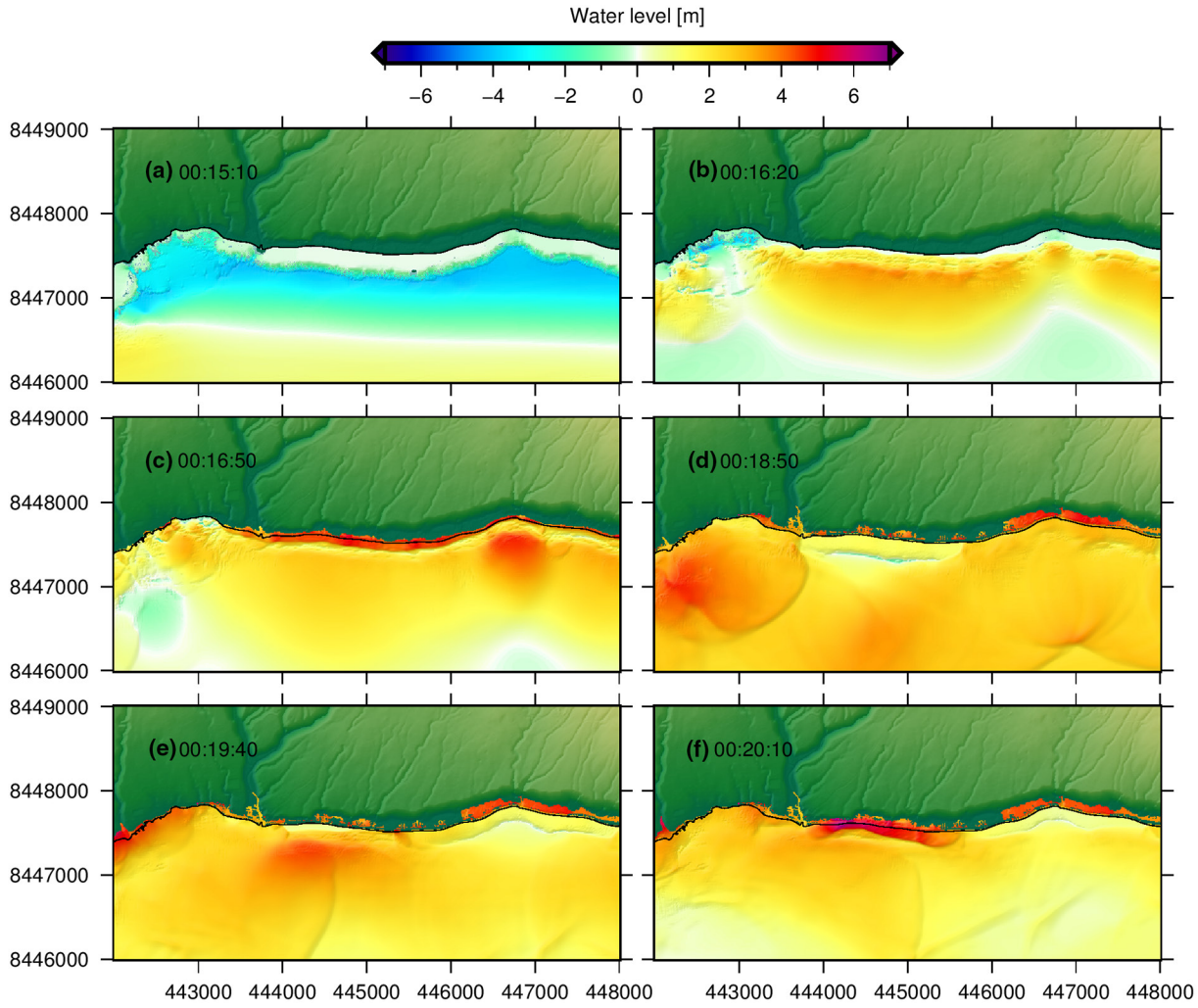

Figure 8. Sequence of inundation due to the first tsunami wave for scenario Lay et al. (2010) Version C at Lepa and Saleapaga. The leading trough is represented by the initial draw-down of the first waves drying out the lagoon and reef foreshore, with the crest rising offshore.

the reef system (e.g., Gelfenbaum et al., 2011), are crucial local drivers of extreme runup and coastal flooding. Furthermore, they support suggestions by Baba et al. (2008) that narrow fringing reefs do not have the width to dissipate wave energy compared with wider reefs. Although, in some circumstances, wider reefs may also increase the wave height through resonant interactions.

Interestingly, in the case of Lay et al. (2010) Version C scenario, waves triggered by the normal fault rupture alone can explain most of the large runup observed in most of southeast Upolu (Figure 9). However, the normal fault alone can only explain 40%–70% of the maximum water level offshore, and does not adequately account for the observed runup in Lepa or in the area between Poutasi and Satalo, or the east-facing region of the coast. Longer wave periods associated with the thrust rupture are amplified more significantly by the local bathymetry at these locations compared with the shorter period waves produced by the normal fault. This highlights how shorter tsunami waves get more easily trapped on narrow reefs and longer tsunami waves are more easily trapped on wider reefs. Nevertheless, our observations corroborate that tsunamis are highly sensitive to source parameters, with significant spatial inundation variability for a given source model. In addition, the observations suggest that one-dimensional tsunami attenuation modeling of offshore wave heights at coast, which is sometimes used to estimate tsunami inundation hazard, is not adequate for use in reef fringed islands (e.g., Smart et al., 2015).

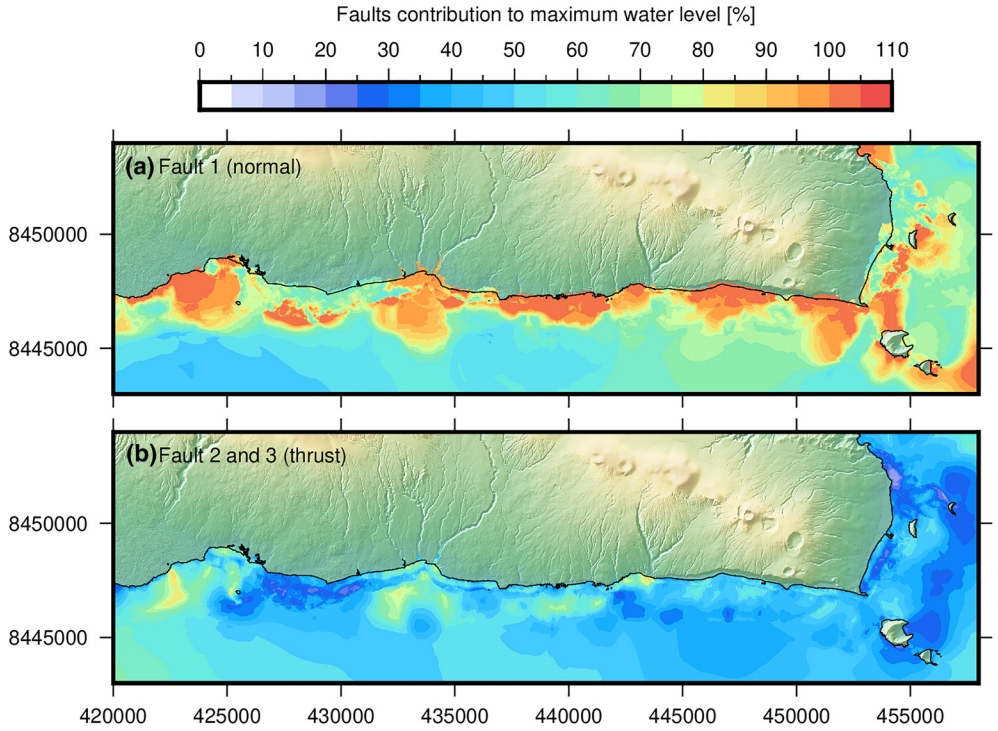

Figure 9. (a) Spatial distribution of Fault 1 (Normal fault) contribution to maximum runup. (b) Spatial distribution of Faults 2 and 3 (Reverse faults) contribution to maximum runup for scenario Lay et al. (2010) Version C. Areas of orange/red are where the normal fault alone contributes to most/all of the inundation. Areas of blue/green are where thrust faults contributed 50%/30% of the runup.

5.2. Refinement of Source Mechanism and Numerical Modeling

Previous investigations of the 2009 SPT source were unable to simulate inundation in Samoa due to the lack of high resolution bathymetric and LiDAR topographic data. The analysis presented in this study shows that each source generates a significantly different tsunami. The Lay et al. (2010) Version C and Hossen et al. (2017) sources produce the most consistent agreement with tsunami records including observed runup in Upolu, Manono and Savaii and the recorded at the Apia tide gauge and DARTs. However, the inability of any of the scenarios tested to adequately capture the extreme runup (~14 m) observed at Lepa on southeast Upolu implies a consistent deficiency in the sources tested and limitations in the numerical modeling approach.

This deficiency is unlikely to be resolved by testing additional uniform slip scenarios. For example, decreasing the strike of the normal fault, could focus more energy and send larger waves toward southeast Upolu, but this would also lead to larger waves reaching the Apia tide gauge, worsening the agreement there. Doing so would also decrease the tsunami wave reaching American Samoa. This would be inconsistent with previous findings that showed even simple sources involving only the normal fault could reproduce runup and tide gauge measurements in Pago Pago (Dilmen et al., 2018; Roeber et al., 2010). It is also likely that a model with frequency dispersion would improve simulation of extreme runup driven by a steep leading trough (e.g., Bai et al., 2018). This would also allow weakly dispersive, short-period waves to propagate from the source to Samoa and amplification of these harmonics to be captured at the coast. These extreme runups could also be due to sloshing of the incoming wave or channeling of waves along gullies that are not adequately represented in the DEM (e.g., Smart et al., 2018) and the 10 m grid resolution. It is also possible that the LiDAR data is not fully representative of the preevent onshore terrain prior to postdisaster reconstruction and modification of local topography.

Heterogeneous rupture with variable slip distribution could also reconcile different issues in the scenarios used here. For example, a finite-fault model of the normal fault presented in Lay et al. (2010) in-

dicate larger slip patches west and east of the epicenter. This could provide additional tsunami energy toward Upolu while maintaining high tsunami energy toward Tutuila and limiting the amount of wave energy traveling to the Apia tide gauge in between the two islands. The short-period waves generated from a variable slip rupture may excite the resonance modes in Lepa and Lalomanu and increase the computed runup to better match the observations. Hence, future investigation using a nonhydrostatic model and considering heterogeneous rupture with a variable slip distribution, as well as stochastic source modeling and higher resolution simulation grid (e.g., Davies et al., 2019; De Risi & Goda, 2017; L. Li et al., 2016; Yamazaki et al., 2018), might improve the inundation and runup presented in this study.

Notwithstanding, the model results show high spatial variability of runup and flow depths similar to the surveyed data, with areas of highest runup observed in southeast Upolu. Our results suggest variability is driven by the rupture source configuration and localized tsunami amplifications due to complex bathymetry within the fringing reef and along coastal topography.

This study highlights that good fits to the DART buoy data does not always guarantee accurate representation of runup, particularly where the buoys are situated away from the main tsunami energy beams. Runup computations also have uncertainties due to model approximation and resolution that account for some of the discrepancies. Nevertheless, this comparative study demonstrates the use of tsunami simulation to model surveyed runup and instrumentally recorded coastal and deep-ocean observations to better constrain the source. This approach, however, is highly reliant on available high-resolution topography and nearshore bathymetry data for tsunami-affected shorelines. Future LiDAR topography and bathymetry acquisition for the northern Tonga Islands could provide a basis to re-evaluate the 2009 SPT following the above recommendations and expand reconstruction of propagation and inundation to all three impacted island groups: Samoa, American Samoa, and northern Tonga. Runup information from all three countries would provide better constraints for validation of finite-fault and nonhydrostatic models of the tsunami source.

6. Conclusions

This study has reconstructed the 2009 SPT in Samoa to observe wave characteristics and evaluate the physical factors affecting the observed inundation in southeast Upolu. We applied BG-Flood to simulate the tsunami from initiation through propagation to inundation for 14 possible sources of the event and evaluated agreement against instrumental records and observed runup. Two source models performed better overall with moderate agreement with the DART and Apia tide gauge records, and good agreement with observed runup on Upolu, Manono, and Savaii islands. While our model reproduces the runup along most of southeast Upolu (9 m), it does not capture the extreme runup record (14 m). This might in part be due to source complexities which are not represented using a uniform slip model, and limitations in the selected models. Run-up calculations also have uncertainties and even well-constrained source models can sometimes fail to fully account for observed run-up given limitations in bathymetry and approximations in numerical modeling methods. Analysis of the relative contributions of the normal and thrust faulting for this doublet event on tsunami behavior indicates that the normal fault alone can explain up to ~70% of the observed runup and flow depths up to 5 m on southeast Upolu.

Our findings indicate that inundation observed in Samoa is sensitive to the source rupture in addition to localized topographic and bathymetric features. The source details control the frequency contents of the tsunami and the fringing reefs control the resonance modes and periods. If the two constructively interfere, as was the case for the 2009 SPT along southeast Upolu, the impacts become much more severe than expected. The narrow fringing reef and constricted onshore geomorphology on southeast Upolu also plays a major role in exacerbating wave runup and flow depth along this coast. The use of a nonhydrostatic model can account for dispersion of short-period tsunami waves as well as vertical flow inertia on steep slopes to reduce uncertainties in runup computations. Future simulation of runup in all three countries impacted by the event (Samoa, American Samoa, and Tonga) will enable iterative refinement of the source mechanism and nearshore effects to regional inundation distribution.

Data Availability Statement

BG-Flood model is open-source and available at (https://github.com/CyprienBosserelle/BG_Flood), and the code version used in this research is archived at (http://doi.org/10.5281/zenodo.3905416). The supporting simulation video is available at (https://doi.org/10.5281/zenodo.4054271). LiDAR data were provided by the Samoa Ministry of Natural Resources and Environment (MNRE), Disaster Management Office through the Pacific Risk Tools for Resilience Project, and is available through MNRE via formal request. DART data used in this study were obtained from the U.S. National Oceanic and Atmospheric Administration, National Geophysical Data Center website: https://www.ngdc.noaa.gov/hazard/dart/2009samoa_dart.html. Tide gauge data were obtained from the Australian Bureau of Meteorology, Tides Unit through the Pacific Sea Level and Geodetic Monitoring project as part of Climate and Oceans Support Program in the Pacific, and is also available from the U.S. National Tsunami Warning Center (https://ntwc.ncep.noaa.gov/previous.events/?p=09-29-09-Samoa). This study utilized the Generic Mapping Tools (GMT) for data processing and presentation.

Acknowledgments
This research was supported by the New Zealand National Institute of Water and Atmospheric Research (NIWA) Taihoro Nukurangi through Strategic Science Investment Fund Project Nos. CARH2002, CARH2006, and PRAS2001 (S. Williams, C. Bosserelle, R. Paulik, and E. Lane). K. F. Cheung and Y. Yamazaki received support from the U.S. National Oceanic and Atmospheric Administration Grant No. NA19NWS4670012 and T. Lay's earthquake research was supported by the U.S. National Science Foundation (Grant EAR1802364). V. Roeber acknowledges financial support from the Isite program Energy Environment Solutions (E2S), the Communauté d'Agglomération Pays Basque (CAPB), and the Communauté Région Nouvelle Aquitaine (CRNA) for the chair HPC-Waves. We thank the two anonymous reviewers for their helpful feedback which improved the paper.

References

Abe, K. (2011). Synthesis of a tsunami spectrum in a semi-enclosed basin using its background spectrum. *Pure and Applied Geophysics*, *168*, 1101–1112. https://doi.org/10.1007/s00024-010-0222-x

Baba, T., Mleczko, R., Burbridge, D., Cummins, P. R., & Thio, H. K. (2008). The effect of the Great Barrier Reef on the propagation of the 2007 Solomon Islands tsunami recorded in Northeastern Australia. *Pure and Applied Geophysics*, *165*, 2003–2018. https://doi.org/10.1007/s00024-008-0418-5

Bai, Y., & Cheung, K. F. (2016). Hydrostatic versus non-hydrostatic modeling of tsunamis with implications for insular shelf and reef environments. *Coastal Engineering*, *117*, 32–43.

Bai, Y., Yamazaki, Y., & Cheung, K. F. (2018). Amplification of drawdown and runup over Hawaii's insular shelves by tsunami N-waves from mega Aleutian earthquakes. *Ocean Modelling*, *124*, 61–74.

Bassett, D., Kopp, H., Sutherland, R., Henrys, S. A., Watts, A. B., Timm, C., et al. (2016). Crustal structure of the Kermadec arc from MANGO seismic refraction profiles. *Journal of Geophysical Research: Solid Earth*, *121*(10), 7514–7546. https://doi.org/10.1002/2016JB013194

Beavan, J., Wang, X., Holden, C., Wilson, K., Power, W., Prasetya, G., et al. (2010). Near-simultaneous great earthquakes at Tongan megathrust and outer rise in September 2009. *Nature*, *466*, 959–963.

Bevis, M., Taylor, F. W., Schutz, B. E., Recy, J., Isacks, B. L., Helu, S., et al. (1995). Geodetic observations of very rapid convergence and back-arc extension at the Tonga arc. *Nature*, *374*, 249–251. https://doi.org/10.1038/374249a0

Buckley, M., Lowe, R., Hansen, J., van Dongeren, A., & Storlazzi, C. (2018). Mechanisms of wave-driven water level variability on reef-fringed coastlines. *Journal of Geophysical Research: Oceans*, *123*, 3811–3831. https://doi.org/10.1029/2018JC013933

Chang, S.-J., Ferreira, A., & Faccenda, M. (2016). Upper- and mid-mantle interaction between the Samoan plume and the Tonga–Kermadec slabs. *Nature Communications*, *7*, 1–9. https://doi.org/10.1038/ncomms10799

Cheung, K. F., Bai, Y., & Yamazaki, Y. (2013). Surges around the Hawaiian Islands from the 2011 Tohoku Tsunami. *Journal of Geophysical Research: Oceans*, *118*(10), 5703–5719. https://doi.org/10.1002/jgrc.20413

Clark, K., Power, W., Nishimura, Y., Kautoke,R. 'A., Vaiomo'unga, R., Pongi, 'A., & Fifita, M. (2011). Characteristics of the 29th September 2009 South Pacific tsunami as observed at Niuatoputapu Island, Tonga. *Earth-Science Reviews*, *107*, 52–65. https://doi.org/10.1016/j.earscirev.2010.12.001

Craig, T. J., Copley, A., & Jackson, J. (2014). A reassessment of outer-rise seismicity and its implications for the mechanics of oceanic lithosphere. *Geophysical Journal of International*, *197*(1), 63–89. https://doi.org/10.1093/gji/ggu013

Davies, G. (2019). Tsunami variability from uncalibrated stochastic earthquake models: Tests against deep ocean observations 2006-2016. *Geophysical Journal International*, *218*, 1939–1960. https://doi.org/10.1093/gji/ggz260

De Risi, R., & Goda, K. (2017). Simulation-based probabilistic tsunami hazard analysis: Empirical and robust hazard predictions. *Pure and Applied Geophysics*, *174*, 3083–3106. https://doi.org/10.1007/s00024-017-1588-9

Dilmen, D. I., Roe, G. H., Wei, Y., & Titov, V. V. (2018). The role of near-shore bathymetry during tsunami inundation in a reef island setting: A case study of Tutuila Island. *Pure and Applied Geophysics*, *175*, 1239–1256. https://doi.org/10.1007/s00024-018-1769-1

Dilmen, D. I., Titov, V. V., & Roe, G. H. (2015). Evaluation of the relationship between coral damage and tsunami dynamics; case study: 2009 Samoa tsunami. *Pure and Applied Geophysics*, *172*, 3557–3572. https://doi.org/10.1007/s00024-015-1158-y

Dudley, W., Whitney, R., Faasisila, J., Fonolua, S., Jowitt, A., & Chan-Kau, M. (2011). Learning from the victims: New physical and social science information about tsunamis from victims of the September 29, 2009 event in Samoa and American Samoa. *Earth-Science Reviews*, *107*, 201–206. https://doi.org/10.1016/j.earscirev.2011.03.005

Duputel, Z., Kanamori, H., Tsai, V. C., Rivera, L., Meng, L., Ampuero, J.-P., et al. (2012). The 2012 Sumatra great earthquake sequence. *Earth and Planetary Science Letters*, *351–352*, 247–257. https://doi.org/10.1016/j.epsl.2012.07.017

Fan, W., Shearer, P. M., Ji, C., & Bassett, D. (2016). Mulitple branching rupture of the 2009 Tonga-Samoa earthquake. *Journal of Geophysical Research: Solid Earth*, *121*, 5809–5827. https://doi.org/10.1002/2016JB012945

Franchello, G., & Annunziato, A. (2012). The Samoa Tsunami of 29 September 2009 – early warning system and inundation assessment. *Science of Tsunami Hazards*, *31*(1), 19–61.

Fritz, H. M., Borrero, J. C., Synolakis, C. E., Okal, E. A., Weiss, R., Titov, V. V., et al. (2011). Insights on the 2009 South Pacific tsunami in Samoa and Tonga from field surveys and numerical simulations. *Earth-Science Reviews*, *107*, 66–75. https://doi.org/10.1016/j.earscirev.2011.03.004

FUGRO. (2016). *Report of survey: Airborne Lidar bathymetric and Topographic Survey of Samoa 2015, Contract: ECRCR-LIB 2.1, Fugro LADS Document Reference No: TLCS00.047.008, Issue No: 1.00*. Kidman Park, SA: Fugro LADS Corporation Pty Ltd.

Gawehn, M., van Dongeren, A., van Rooijen, A., Storlazzi, C. D., Cheriton, O. M., & Reniers, A. (2016). Identification and classification of very low frequency waves on a coral reef flat. *Journal of Geophysical Research: Oceans*, *121*, 7560–7574. https://doi.org/10.1002/2016JC011834

Gelfenbaum, G., Apotsos, A., Stevens, A., & Jaffe, B. (2011). Effects of fringing reefs on tsunami inundation: American Samoa. *Earth-Science Reviews*, *107*, 12–22. https://doi.org/10.1016/j.earscirev.2010.12.005

Goff, J., & Dominey-Howes, D. (Eds.). (2011). The 2009 South Pacific tsunami. *Earth-Science Reviews*, *107*, v–vii. https://doi.org/10.1016/j.earscirev.2011.03.006

Govers, R., & Wortel, M. (2005). Lithosphere tearing at STEP faults: Response to edges of subduction zones. *Earth and Planetary Science Letters*, *236*(12), 505–523. https://doi.org/10.1016/j.epsl.2005.03.022

Gurnis, M., Ritsema, J., Van Heijst, H. J., & Zhong, S. (2000). Tonga slab deformation: The influence of a lower mantle upwelling on a slab in a young subduction zone. *Geophysical Research Letter*, *27*, 2373–2376. https://doi.org/10.1029/2000GL011420

Han, S.-C., Sauber, J., Pollitz, F., & Ray, R. (2019). Sea level rise in the Samoan Islands escalated by viscoelastic relaxation after the 2009 Samoa-Tonga Earthquake. *Journal of Geophysical Research: Solid Earth*, *124*(4), 4142–4156. https://doi.org/10.1029/2018JB017110

Hossen, M. J., Gusman, A. R., Satake, K., & Cummins, P. R. (2017). An adjoint sensitivity method applied to time reverse imaging of tsunami source for the 2009 Samoa earthquake. *Geophysical Research Letters*, *45*, 627–636. https://doi.org/10.1002/2017GL076031

Kiser, E., & Ishii, M. (2012). Combining seismic arrays to image the high-frequency characteristics of large earthquakes. *Geophysical Journal International*, *188*(3), 1117–1128. https://doi.org/10.1111/j.1365-246X.2011.05299.x

Konter, J., & Jackson, M. (2012). Large volumes of rejuvenated volcanism in Samoa: Evidence supporting a tectonic influence on late-stage volcanism. *Geochemistry, Geophysics, Geosystems*, *13*, Q0AM04. https://doi.org/10.1029/2011gc003974

Koppers, A. A. P., Russell, J., Jackson, M. G., Konter, J., Staudigel, H., & Hart, S. R. (2008). Samoa reinstated as a primary hotspot trail. *Geology*, *36*(6), 435–438. https://doi.org/10.1130/G24630A.1

Koppers, A. A. P., Russell, J. A., Roberts, J., Jackson, M. G., Konter, J. G., Wright, D. J., et al. (2011). Age systematics of two young en-echelon Samoan volcanic trails. *Geochemistry, Geophysics, Geosystems*, *12*, Q07025. https://doi.org/10.1029/2010GC003438

Krüger, J., & Kumar, S. (2008). Samoa Technical Report: High-resolution bathymetric survey. EU-SOPAC Project Report ER 112, Pacific Islands Applied Geoscience Commission, Suva, Fiji.

Lay, T., Ammon, C. J., Kanamori, H., Rivera, L., & Koper, K. D. (2010). The 2009 Samoa-Tonga great earthquake triggered doublet. *Nature*, *466*, 964–968. https://doi.org/10.1038/nature09214

Li, L., Lay, T., Cheung, K. F., & Ye, L. (2016). Joint modeling of teleseismic and tsunami wave observations to constrain the 16 September 2015 Illapel, Chile Mw 8.3 earthquake rupture process. *Geophysical Research Letters*, *43*(9), 4303–4312. https://doi.org/10.1002/2016GL068674

Li, X., Shao, G., & Ji, C. (2009). Rupture process of Mw 8.1 Samoa earthquake constrained by joint inverting teleseismic body, surface waves and local strong motion. *EOS Transactions*, *90*(53), U21D-03.

Meng, Q., Heeszel, D. S., Ye, L., Lay, T., Wiens, D. A., Jia, M., et al. (2015). The 3 May 2006 (M_W 8.0) and 19 March 2009 (M_W 7.6) Tonga earthquakes: Intraslab compressional faulting below the megathrust. *Journal of Geophysical Research: Solid Earth*, *120*, 6297–6316. https://doi.org/10.1002/2015JB012242

Millen, D. W., & Hamburger, M. W. (1998). Seismological evidence for tearing of the Pacific plate at the northern termination of the Tonga subduction zone. *Geology*, *26*(7), 659–662. https://doi.org/10.1130/0091-7613

Nealy, J. L., & Hayes, G. P. (2015). Double point source W-phase inversion: Real-time implementation and automated model selection. *Physics of the Earth and Planetary Interiors*, *249*, 68–81. https://doi.org/10.1016/j.pepi.2015.09.005

Okada, Y. (1985). Surface deformation due to shear and tensile faults in a half space. *Bulletin of the Seismological Society of America*, *75*(4), 1135–1154.

Okada, Y. (1992). Internal deformation due to shear and tensile fault in a half space. *Bulletin of the Seismological Society of America*, *82*(2), 1018–1040.

Okal, E. (1992). Use of the mantle magnitude Mm for the reassessment of the moment of historical earthquakes, I: Shallow events. *Pure and Applied Geophysics*, *139*, 17–57.

Okal, E., Borrero, J., & Chagué-Goff, C. (2011). Tsunamigenic predecessors to the 2009 Samoa earthquake. *Earth-Science Reviews*, *107*, 127–140.

Okal, E. A., Fritz, H. M., Synolakis, C. E., Borrero, J. C., Weiss, R., Lynett, P. J., et al. (2010). Field survey of the Samoa tsunami of 29 September 2009. *Seismological Research Letters*, *81*(4), 577–591.

Pawlowicz, R., Beardsley, B., & Lentz, S. (2002). Classical tidal harmonic analysis with error analysis in MATLAB using T_TIDE. *Computers & Geosciences*, *28*, 929–937. https://doi.org/10.1016/S0098-3004(02)00013-4

Popinet, S. (2011). Quadtree-adaptive tsunami modeling. *Ocean Dynamics*, *61*(9), 1261–1285. https://doi.org/10.1007/s10236-011-0438-z

Popinet, S. (2012). Adaptive modeling of long-distance wave propagation and fine-scale flooding during the Tohoku tsunami. *Natural Hazards and Earth System Sciences*, *12*(4), 1213–1227. https://doi.org/10.5194/nhess-12-1213-2012

Reese, S., Bradley, B. A., Bind, J., Smart, G., Power, W., & Sturman, J. (2011). Empirical building fragilities from observed building damage in the 2009 South Pacific tsunami. *Earth-Science Reviews*, *107*, 156–173. https://doi.org/10.1016/j.earscirev.2011.01.009

Roeber, V., Yamazaki, Y., & Cheung, K. F. (2010). Resonance and impact of the 2009 Samoa tsunami around Tutuila. *Geophysical Research Letters*, *37*, L21604. https://doi.org/10.1029/2010GL044419

Smart, G. (2017). Improving Flood hazard prediction models. *International Journal of River Basin Management*, *16*, 449–456. https://doi.org/10.1080/15715124.2017.1411923

Smart, G. (2018). LiDAR resolution for catchment-inclusive hydrodynamic models. River Flow 2018, E3S Web of Conferences, 40, 06031. https://doi.org/10.1051/e3sconf/20184006031

Smart, G., Crowley, K., & Lane, E. (2015). Estimating tsunami run-up. *Natural Hazards*, *80*, 1933–1947. https://doi.org/10.1007/s11069-015-2052-8

Tang, L., Titov, V., & Chamberlin, C. (2009). Development, testing, and applications of site-specific tsunami inundation models for real-time forecasting. *Journal of Geophysical Research*, *114*, (C12025). https://doi.org/10.1029/2009JC005476

Vacondio, R., Palù, A., Ferrari, A., Mignosa, P., Aureli, F., & Dazzi, S. (2017). A non-uniform efficient grid type for GPU-parallel Shallow Water Equations models. *Environmental Modelling & Software*, *88*, 119–137. https://doi.org/10.1016/j.envsoft.2016.11.012

Williams, S. (2019). Tsunami elemental signatures in the Samoan Islands: A case study. In L. F. Mazadiego, E. D. M. Garcia, F. Barro-Parra, & M. Izquierdo-Díaz (Eds.), *Applied geochemistry with case studies on geological formations, exploration techniques and environmental issues* (pp. 1-12). InTech Open. https://doi.org/10.5772/intechopen.85639

Willmott, C., Robeson, S., & Matsuura, K. (2012). A refined index of model performance. *International Journal of Climatology*, *32*, 2088–2094. https://doi.org/10.1002/joc.2419

Wilson, K. J., Power, W. L., Nishimura, Y., Kautoke, R. 'A., Vaiomo'unga, R., Mori'A. Pongi, H., et al. (2009). Post-tsunami survey of Niuatoputapu island, Tonga, following the 30th September, 2009, South Pacific tsunami. GNS Science Report 2009/71. Lower Hutt, NZ: GNS Science.

Wood, N., Jones, J., Yamazaki, Y., Cheung, K. F., Brown, J., Jones, J., et al. (2018). Population vulnerability to tsunami hazards informed by previous and projected disasters: A case study of American Samoa. *Natural Hazards*, *95*, 505–528. https://doi.org/10.1007/s11069-018-3493-7

Yamazaki, Y., Cheung, K. F., & Kowalik, Z. (2011). Depth-integrated, non-hydrostatic model with grid nesting for tsunami generation, propagation, and run-up. *International Journal for Numerical Methods in Fluids*, *67*(12), 2081–2107.

Yamazaki, Y., Cheung, K. F., & Lay, T. (2018). A self-consistent fault-slip model for the 2011 Tohoku earthquake and tsunami. *Journal of Geophysical Research: Solid Earth*, *123*(2), 1425–1458. https://doi.org/10.1002/2017JB014749

Zhou, H., Wei, Y., & Titov, V. V. (2012). Dispersive modeling of the 2009 Samoa tsunami. *Geophysical Research Letters*, *39*, L16603. https://doi.org/10.1029/2012GL053068